

# From Canopy to Ground via ForestGen3D: Learning Cross-Domain Generation of 3D Forest Structure from Aerial-to-Terrestrial LiDAR

Juan Castorena<sup>a</sup>, E. Louise Loudermilk<sup>b</sup>, Scott Pokswinski<sup>c</sup>, Rodman Linn<sup>a</sup>

<sup>a</sup>Los Alamos National Laboratories, Los Alamos, NM, 48124 USA

<sup>b</sup>Southern Research Station, Disturbance and Prescribed Fire Laboratory, 320 E Green St., Athens, GA 30606.

<sup>c</sup>New Mexico Consortium, 4200 W Jemez Rd 200, Los Alamos, NM 87544

---

## Abstract

The 3D structure of living and non-living components in ecosystems plays a critical role in determining ecological processes and feedbacks from both natural and human-driven disturbances. Anticipating the effects of wildfire, drought, disease, or atmospheric deposition depends on accurate characterization of 3D vegetation structure, yet widespread measurement remains prohibitively expensive and often infeasible. We introduce ForestGen3D, a novel generative modeling framework that synthesizes high-fidelity 3D forest structure using only aerial LiDAR (ALS) inputs. ForestGen3D is based on conditional denoising diffusion probabilistic models (DDPMs) trained on co-registered ALS/TLS (terrestrial LiDAR) data. The model learns to generate TLS-like 3D point clouds conditioned on sparse ALS observations, effectively reconstructing occluded sub-canopy detail at scale. To ensure ecological plausibility, we introduce a geometric containment prior based on the convex hull of ALS observations and provide theoretical and empirical guarantees that generated structures remain spatially consistent. We evaluate ForestGen3D at tree, plot, and landscape scales using real-world data from mixed conifer ecosystems, and show that it produces high-fidelity reconstructions that closely match TLS references in terms of geometric similarity and biophysical metrics, such as tree height, DBH, crown diameter and crown volume. Additionally, we demonstrate that the containment property can serve as a practical proxy for generation quality in settings where TLS ground truth is unavailable. Our results position ForestGen3D as a scalable tool for ecological modeling, wildfire simulation, and structural fuel characterization in ALS-only environments.

*Keywords:* Forests, 3D generation, artificial intelligence, terrestrial, aerial, LiDAR, denoising diffusion, remote sensing, wildfires.

---

## 1. Introduction

Wildfires, drought, pathogens, and other natural disturbances are increasingly transforming forested landscapes, driving the need for improved ecological monitoring and fuel structure characterization. These disturbances are shaped not only by vegetation type but also by the three-dimensional (3D) arrangement of biomass across vertical and horizontal layers. The 3D structure of both living and non-living components of vegetation plays a critical role in regulating ecological processes, including energy and moisture fluxes, carbon storage, and fire behavior. However, large-scale collection of detailed 3D vegetation structure remains a major bottleneck. Most landscape-scale ecological assessments still rely on field plots that are statistically upscaled using summary metrics. To spatially represent forests, synthetic layouts are often generated by populating plots with idealized geometric models (e.g., cylinders, ovals), randomly placed according to field statistics [1, 2, 3, 4]. While informative, these methods often overlook spatial relationships between vegetation components and fail to capture the full 3D spatial heterogeneity, both of which are crucial for modeling dynamic ecological processes. A related class of methods common in visualization, and gaming applications uses procedural forest generation, where tree forms and vegetation distributions are instantiated from parametric rules or stylized templates. Tools such as SpeedTree [5] and Unity's Terrain Engine [6] exemplify this approach, offering efficient generation of stylized vegetation for rendering purposes. While these models can quickly populate large virtual landscapes, they typically prioritize visual coherence and rendering performance over fidelity

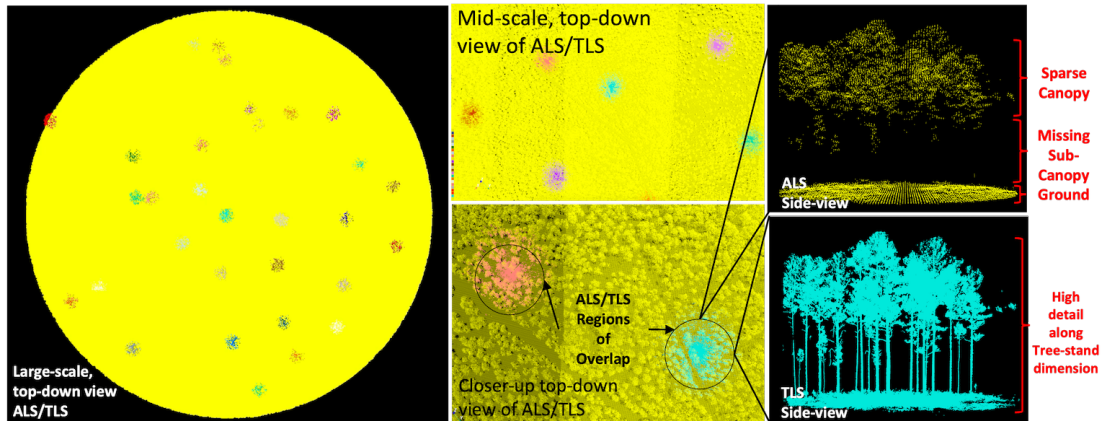


Figure 1: Characteristics of ALS (in yellow) and TLS data at a surveying forest site, covering 2.5 km in diameter with 31 TLS scans randomly distributed (a color-coded blob per scan). Overlapping ALS in top-right shows a side-view point cloud with sparse/missing information below the canopy. Co-registered TLS in the bottom-right, on the other hand shows high detail along the tree-stand direction but is limited in the lat-long direction due to physical range limitations of TLS (as shown in the top-down images).

with real-world forest conditions, and are therefore less suitable for scientific analyses that depend on detailed and ecologically grounded 3D representations of forest fuel structure.

Over the past two decades, 3D remote sensing technologies particularly terrestrial laser scanning (TLS) [7] and aerial laser scanning (ALS) [8] have become increasingly valuable for vegetation mapping. TLS offers high-resolution 3D point clouds of stems, understory, and ground structure but is constrained to plot-scale deployment due to cost and labor demands. ALS, by contrast, provides broad landscape coverage and effectively captures canopy structure but suffers from occlusion and fails to resolve sub-canopy features in dense forests, even in full-waveform systems [9, 10, 11]. These limitations are illustrated in Fig.1: while ALS provides landscape-scale coverage of the upper canopy, TLS offers detail below the canopy but lacks coverage in the lateral/longitudinal directions. Surprisingly, most methods in forest mapping and monitoring do not exploit the complementary nature of these two sensing modalities. Instead, they typically rely on either ALS or TLS independently, developing analysis pipelines tailored to a single data source. This leads to structural blind spots for instance, missing understory in ALS-based workflows or extrapolated spatial sparsity in TLS-based ones that fail to respect landscape heterogeneity and that persist in operational products and ecological models [12, 13].

In this work, we propose to bridge these sensing gaps by learning generative models of 3D fuel structure that leverage the strengths of both data sources. To achieve this, we develop ForestGen3D, a cross-domain generative modeling framework based on denoising diffusion probabilistic models (DDPMs). These models are trained here on a new dataset of co-registered ALS/TLS tree 3D point clouds referred to as the *CoLiDAR Forest3D (ALS/TLS)* and collected across mixed conifer vegetation ecosystems. Once trained, the model can generate novel 3D vegetation samples by starting from random noise and iteratively refining structure through a learned denoising process, guided by ALS input as shown in Fig. 2. To the best of our knowledge, this is the first approach to leverage conditional diffusion models for cross-domain generation of 3D forest structure, bridging the gap between sparse, landscape-scale ALS and detailed, plot-scale, TLS representations. This enables scalable ecological modeling of forests in full vertical profile beyond existing upsampling or procedural simulation methods.

Existing 3D generative and completion models, such as PCN [14], 3D-GAN [15], latent-GAN [16], and PointFlow [17], have so far been developed and tested primarily on man-made objects from synthetic datasets such as ShapeNet. While effective in those controlled domains, their suitability for modeling real-world forest vegetation remains largely unknown. Forest structure presents fundamentally different challenges: complex topologies with intertwined crowns, occlusion-driven sparsity due to canopy cover, and vertical heterogeneity across understory, stems, and crowns. These characteristics may degrade the performance of models designed for compact, uniformly sampled shapes. Moreover, existing methods are typically trained without reference to real-world sensing modalities such as LiDAR, and therefore do not account for the anisotropic density, partial observability, and sensor-specific artifacts present in ecological

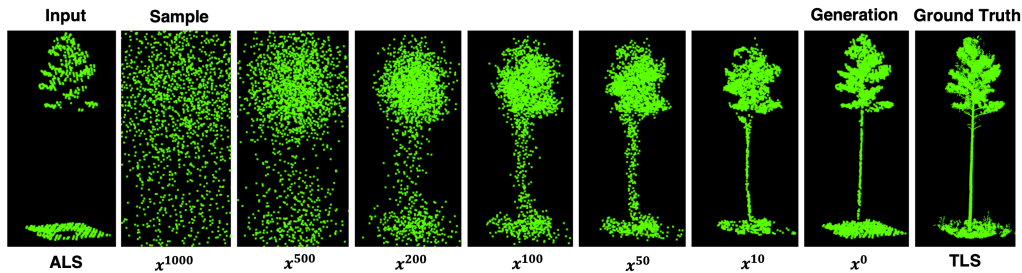


Figure 2: Denoising Diffusion Probabilistic Model (DDPM) in Action. DDPM iteratively denoises a sample guided by ALS measurements and generates a sample of forest tree 3D structure from the learned training distribution. Note that the 3D structural information provided by ALS is effective for constraining 3D structural generation in the vertical tree stand direction.

data. In contrast, the objective of our approach is to generate ecologically realistic 3D vegetation structure directly from ALS/TLS data collected in mixed conifer forests, capturing both the natural variability of vegetation and the sensor-dependent effects inherent in terrestrial and airborne LiDAR measurements.

In the sections that follow, we present our dataset and training approach, describe the DDPM-based model, and evaluate ForestGen3D across tree, plot, and landscape scale experiments. Quantitative and qualitative results demonstrate that our approach approximates TLS-level structural detail using ALS data alone, enabling scalable forest modeling for applications in fire science, ecological monitoring, and remote sensing.

## 2. ForestGen3D

The core problem we address is generating synthetic forests by improving the fidelity of individual tree structures beyond conventional coarse-shape models. To achieve this, we explicitly preserve ecosystem fidelity by conditioning the generation process on ALS inputs, which provide canopy-level structure tied to real forest layouts. Rather than modeling entire plots or landscapes directly which can compromise fine-grained detail and impose significant computational demands, we focus on learning 3D structure at the tree scale, where the physical representation of vegetation is most accurate. This localized modeling approach allows for more efficient training and data preparation, reducing the need to capture broad ecosystem variation in a single model. Moreover, it enables scalable deployment by applying the generative model independently to each detected tree at the plot or landscape scale, under the assumption that only regions beneath vegetation are susceptible to occlusion in ALS data. To support this effort, we constructed a 3D forest dataset of co-registered ALS/TLS tree samples, which we used to train cross-domain denoising diffusion probabilistic models (DDPMs). These models learn the statistical distribution of tree 3D structure in a target domain (TLS) conditioned on observations in a reference domain (ALS). DDPMs start from random Gaussian noise and iteratively refine structure through a learned denoising process, enabling flexible and efficient generation of high-resolution 3D tree forms. Fundamentally, the framework learns to generate samples from the TLS distribution conditioned on a measured sample from the ALS distribution. Figure 2 illustrates this process: an ALS input guides the denoising steps, which progressively reconstruct the full 3D structure of a tree, including stem and understory geometry missing from the input.

### 2.1. Training dataset

We construct a new 3D forest dataset *CoLiDAR-Forest3D (ALS/TLS) dataset*, containing 2,900 co-registered TLS/ALS tree scans for training, including both individual trees and clusters of closely packed trees. The dataset was constructed using the co-registration approach from [18] to align TLS scans with overlapping ALS data and the deep-learning-based tree detection method from [19] to extract individual trees. The raw data were collected from a mixed-conifer forest at Fort Stewart in the United States [20], primarily featuring species such as longleaf pine, slash pine, loblolly pine, and turkey oak. The understory consists of graminoids, forbs, and shrubs, including wiregrass, gallberry, and saw palmetto. TLS data was acquired using a Leica BLK360 LiDAR scanner with an 830 nm wavelength laser and a field of view (FOV) of 300° (vertical) and 360° (horizontal). Scans were taken from static tripod positions,

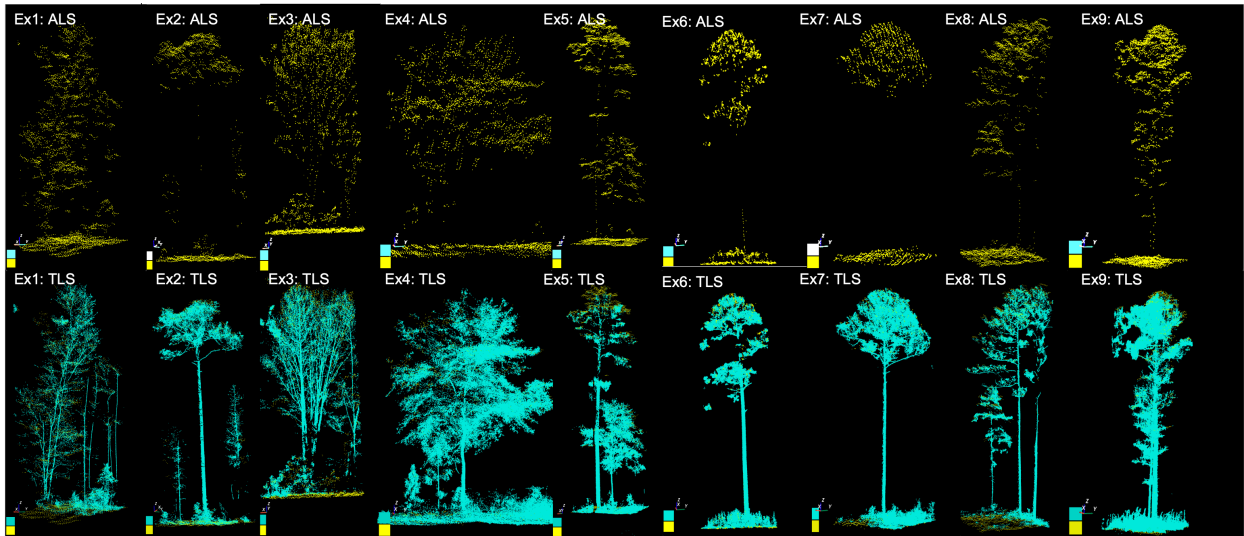


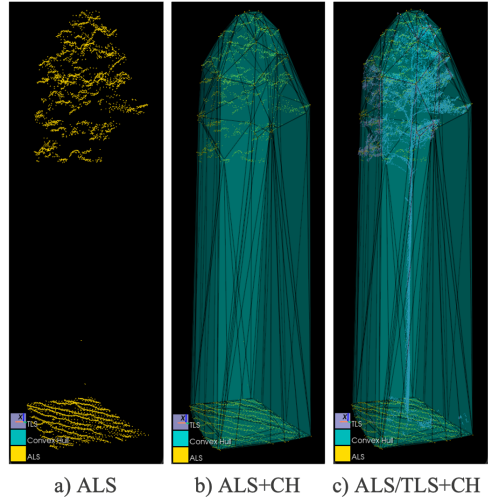
Figure 3: 9 examples of the 3D training dataset consisting of 2900 examples of segmented and co-registered ALS/TLS trees. ALS trees in yellow in the top row, corresponding co-registered TLS trees in aqua color in the bottom row.

with 240 scans randomly distributed across a 2.5 km diameter area. Each TLS scan contained approximately 8 million points, with around 4.6 million from the ground. Since most returns were concentrated within a 25-meter range, points beyond this threshold were removed to mitigate the non-uniform point density. A representative sampling pattern of TLS scans across a region is shown in Fig. 1, where each TLS scan is represented by a color-coded blob. ALS data was collected using a Galaxy T2000 LiDAR sensor mounted on a fixed-wing aircraft. The sensor operates at a 1064 nm wavelength and captures up to eight returns per pulse, with a  $28^\circ$  FOV, flown at an altitude of approximately 1,675 meters. The system achieves a point density of approximately 15 points per square meter and maintains an accuracy of 0.03 to 0.25 meters RMSE within a 150–6,500 meter range. The surveyed area was covered using multiple overlapping flight lines, including seven cross strips to reduce point sparsity and enhance coverage. Unlike TLS, ALS points are not affected by satellite signal occlusion and were globally aligned using a Trimble CenterPoint RTX RTK system for centimeter-level accuracy. A regional-scale ALS point cloud is shown in Fig. 1 in yellow, with orthographic (top-down) views on the left and middle and a side-view on the top right.

Each TLS scan was initially positioned using GPS-based estimates in global coordinates. These positions were used to extract a corresponding 50 meter radius ALS point-cloud subset around each TLS scan center. The automatic and target-less co-registration approach from [18] was applied to refine the position provided by GPS while also aligning the TLS scan to the ALS point-cloud relative to rotations. Each co-registered pair was manually verified by an expert to ensure qualitative alignment between spatial features. Tree detection was performed using the deep learning (DL)-based method from [19], which detects trees or tightly clustered groups of trees/vegetation by fitting 2D bounding boxes from a top-down bird's-eye view and then expanding each bounding box to 3D informed by the lowest-to-highest point elevation difference. This approach ensures that the resulting 3D bounding boxes capture the full vertical extent of vegetation, from the top of the canopy to the lowest ground point. These bounding boxes were used to extract tree-level point clouds by truncating the points in the ALS and TLS scans inside each 3D box. To mitigate the non-uniform point density in TLS, we truncated each point cloud to a 25m radius and downsampled each TLS scan to a 0.10 cm voxel size. Each tree scan was then centered and normalized within the  $[0, 1]^3$  range. The dataset was manually curated to remove incomplete trees (e.g., those significantly cut by bounding boxes), and incorrect detections. The final dataset consists of 2,900 TLS/ALS tree or tree-cluster pairs. Fig. 3 illustrates nine ALS/TLS example pairs, with ALS trees in yellow (top row) and corresponding TLS scans in aqua (bottom row). For validation, we use an additional set of 300 tree samples from the same ecosystem than the training data but that are non-overlapping. These examples were collected using the same TLS and ALS sensors and processed using identical co-registration and tree detection pipelines.

Due to the physical operation principles of LiDAR, TLS and ALS yield structurally complementary but distributionally distinct 3D point cloud characteristics. ALS captures forest structure from an aerial, top-down perspective and provides relatively complete sampling of the upper canopy features, while TLS operates from the ground and more effectively resolves stems, understory and internal structure. This leads to a broader spatial support for ALS compared to TLS. Let  $\mathbf{X} \in \mathbb{R}^{N \times 3}$  and  $\mathbf{Y} \in \mathbb{R}^{M \times 3}$  denote the TLS and ALS point clouds for an individual tree (or small group of trees), and let  $\mathcal{B}_{\text{ALS}} = \text{Conv}(\mathbf{Y})$  be the convex hull (i.e., convex envelope) of the ALS data. *Assumption:* We adopt a localized containment assumption at the individual tree scale, where TLS points are expected to lie within the convex envelope of their corresponding co-registered ALS points with high probability (see Figure 4). This is expressed as:

$$\mathbb{E}_{(\mathbf{X}, \mathbf{Y}) \sim \mathcal{D}} [\mathbb{E}_{\mathbf{x} \sim \mathbf{X}} [\mathbb{1}(\mathbf{x} \in \mathcal{B}_{\text{ALS}})]] \geq 1 - \epsilon \quad (1)$$



for a small constant  $\epsilon \ll 1$ , with  $(\mathbf{X}, \mathbf{Y}) \sim \mathcal{D}$  drawn from the dataset. Here,  $\mathbf{x} \sim \mathbf{X}$  are 3D points uniformly sampled from the TLS point cloud, and  $\mathbb{1}(\cdot)$  is the indicator function. In our empirical analysis of the training *CoLiDAR-Forest3D (ALS/TLS)* dataset, approximately 3.9% of TLS points fall outside the ALS convex hull, i.e.,  $\epsilon = 0.04$ , validating the assumption at the tree scale. We emphasize that this prior is not assumed to hold globally at the plot or landscape scale and that a variety of factors may violate containment. However, the small deviations from containment that may be locally present are expected and well-justified, as they can result from sensor misalignment, resolution differences, vegetation visible from the ground but occluded from the aerial view, and inherent measurement noise in both ALS and TLS systems. Despite these localized discrepancies, the overall containment expectation introduces a geometric prior that is implicitly learned by our conditional generative model. This prior not only helps constrain synthesis within plausible ALS-guided structure, but also provides a useful means of measuring the spatial fidelity of the generated points relative to the ALS envelope.

## 2.2. 3D Cross-domain Denoising Diffusion Generative Models

Denoising diffusion probabilistic models are generative deep neural networks that operate within a variational inference framework [21]. Their primary objective is to learn an approximation of the underlying training data distribution while enabling flexible and efficient sample generation from this learned distribution. In our context, we adopt DDPMs in a *cross-domain* setting, where the goal is to generate TLS-like 3D vegetation structure conditioned on co-registered ALS measurements. This enables the synthesis of dense sub-canopy and near-ground details in regions where ALS data is sparse or occluded. To this end, we train the model to approximate the conditional distribution  $p(\mathbf{X} | \mathbf{Y})$ , where ALS point clouds represent sparse, canopy dominated measurements, and TLS point clouds provide detailed ground-to-canopy interior structural information. During inference, the model begins from isotropic Gaussian noise and iteratively refines the sample using structural cues provided by ALS input, producing 3D point clouds that resemble high-resolution TLS samples respecting ALS fidelity.

The DDPM architecture consists of two components: a forward diffusion process that progressively corrupts the input point cloud  $\mathbf{X}^0 \in \mathbb{R}^{N \times 3}$  over  $T$  steps by multiplying it with a decaying factor while adding Gaussian noise, and a learned reverse process that denoises the corrupted sample back to a clean reconstruction. This yields a training trajectory:  $\mathbf{X}^0 \rightarrow \mathbf{X}^1 \rightarrow \dots \rightarrow \mathbf{X}^T \sim \mathcal{N}(0, \mathbf{I})$ , as the forward (diffusion) process,  $\mathbf{X}^T \rightarrow \mathbf{X}^{T-1} \rightarrow \dots \rightarrow \hat{\mathbf{X}}^0$  as the reverse (denoising) process. The model conditions each denoising step on ALS observations  $\mathbf{Y}$ , enabling it to learn structure consistent with the canopy geometry while generating plausible TLS content beneath. The network uses an encoder-decoder U-Net structure adapted to point clouds [22], where each block is implemented using PointNet++ layers [23]. Conditioning is applied through feature-wise modulation blocks at each level of the hierarchy, allowing ALS input to guide the generation process. A high-level schematic of the model architecture is shown in Fig. 5. The model is trained on point clouds  $\mathbf{X}, \mathbf{Y} \sim p_{\text{data}}(\mathbf{X}, \mathbf{Y}) \in \mathbb{R}^{N \times 3} \times \mathbb{R}^{M \times 3}$ , sampled from aligned TLS/ALS pairs. The forward diffusion process follows a first-order Markov chain by adding Gaussian noise over  $T$  steps (e.g.,  $T = 1000$ ).

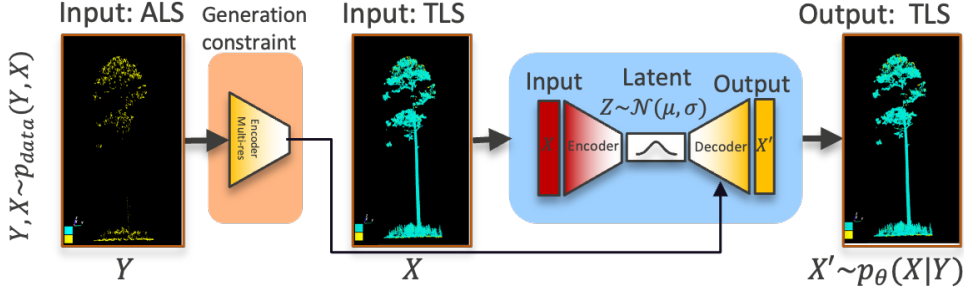


Figure 5: Schematic of ALS-to-TLS cross-domain DDPM. The forward process encodes a TLS sample into Gaussian noise, while the reverse process learns to denoise a sample conditioned on ALS input, reconstructing high-resolution 3D vegetation structure.

The reverse process learns to approximate  $p(\mathbf{X}^{t-1} | \mathbf{X}^t, \mathbf{Y})$ , thereby denoising the latent variable back to a plausible TLS point cloud. Figure 2 illustrates the generative process in a leave-one-out setting, where a withheld TLS scan is reconstructed using only its associated ALS input. The figure shows the denoising trajectory starting from an initial sample  $\mathbf{X}^T \sim \mathcal{N}(0, \mathbf{I})$  and progressively refining toward a tree structure that closely approximates the held-out TLS reference. Notably, the model is able to synthesize sub-canopy features that are missing from the ALS input, highlighting the DDPM’s capacity to infer occluded structural details.

*Remark* (Containment Consistency under ELBO). Because the conditional DDPM is trained via ELBO minimization [21] to approximate the true conditional distribution  $p_{\text{data}}(\mathbf{X} | \mathbf{Y})$ , and the training data satisfies an approximate containment condition at the tree scale, we expect the learned generative model  $p_{\theta}(\mathbf{X} | \mathbf{Y})$  to inherit this spatial bias.

Formally, we can bound the expected point containment (EPC) for tree-level generation as:

$$\mathbb{E}_{\mathbf{Y}} \left[ \mathbb{E}_{\mathbf{X} \sim p_{\theta}(\cdot | \mathbf{Y})} \left[ \mathbb{E}_{\mathbf{x} \sim \mathbf{X}} [1(\mathbf{x} \in \mathcal{B}_{\text{ALS}}(\mathbf{Y}))] \right] \right] \geq 1 - \epsilon - \delta \quad (2)$$

where  $\epsilon$  reflects the empirical containment gap (e.g., 3.9% in our CoLiDAR Forest3D dataset), and  $\delta$  accounts for model approximation error due to ELBO. Since the convex hull is computed per tree (or tight tree cluster), the spatial bias is preserved during training and inference, and we observe in practice that containment violations remain rare and localized. A full proof of Eq. (2) is provided in the Appendix.

### 3. Experimentation

The experiments in this section are designed to address two key questions: (1) Can conditional DDPM models effectively learn the detailed 3D structural distribution of forest vegetation from TLS data with ALS guidance? and (2) Is the approach scalable to plot-scale and landscape-scale deployment, enabling accurate synthesis of tree-level structure and improvement of downstream ecological biometrics commonly used in forest management?. The first set of experiments, presented in Section 3.1, evaluates the generative capacity of DDPMs at the tree scale. We assess whether the model’s inductive biases and architecture are well-suited for representing the hierarchical and self-similar structure of vegetation. This includes analysis of the model’s approximation quality via reconstruction error, as well as ablation studies that explore the sensitivity of generation quality to key DDPM hyperparameters such as diffusion steps. To quantitatively assess reconstruction error, we compute Chamfer Distance (CD) and Earth Mover’s Distance (EMD) between generated and reference TLS point clouds, using held-out tree samples. In addition, we examine the relationship between CD, EMD, and our expected point containment (EPC) metric. The goal of this analysis is to evaluate whether containment can serve as a practical proxy for CD and/or EMD in scenarios where ground-truth TLS data is unavailable. The second set of experiments, detailed in Sections 3.3-3.5, demonstrates the model’s generalization and scalability from tree to landscape scale scenarios in mixed conifer ecosystems. At the tree and plot scales, we evaluate the consistency of ALS-guided generation in matching spatial extents and density patterns observed in ground truth TLS scans. At the regional scale, we deploy the model across 200 meter radius ALS-only regions and assess the realism of synthesized vegetation. For both plot and landscape cases, we compute ecological biometrics including

tree height, diameter at breast height (DBH), crown diameter (CrD), and crown volume (CrV) based on ALS, TLS, ALS+TLS, and ALS+ForestGen3D samples. These comparisons highlight the model’s ability to augment sparse ALS with realistic sub-canopy structure, leading to improved and more complete biometric estimates. Furthermore, we confirm that the containment prior is preserved in inference-time landscape-scale deployments, as evidenced by low out-of-envelope deviation statistics across diverse mixed-conifer landscapes.

### 3.1. Training and Validation

To evaluate the inductive biases and approximation fidelity of our DDPM-based generative framework, we conduct a series of ablation experiments. During training, each batch consists of 16 randomly selected ALS/TLS example pairs. Each point cloud is uniformly subsampled to a fixed size of  $N = 2048$ . This random subsampling enhances dataset diversity by introducing spatial variability across training epochs, enabling the model to encounter a broader range of structural configurations over time. Although the  $N = 2048$  resolution may appear limiting, it applies only at the level of individual trees. When aggregated over larger spatial extents such as plots or landscapes, this per-tree resolution naturally scales to yield detailed reconstructions across entire forested regions. Moreover, higher-resolution representations can be achieved through ensemble sampling, in which multiple stochastic generations are produced for the same conditional ALS input and merged coherently to create denser 3D tree structures. As an illustration of the capabilities of the generative model to approximate 3D tree structures given the existing settings, we include Figure 6 showcasing three examples in the training set with ALS input (first column), AI-generation (second column) and ground truth TLS (third column) in each example. Here, we see that our model is able to generate samples at good qualitative approximations of the 3D structural features of TLS distributions conditional on the ALS inputs across the entire vertical tree-stand direction. Figures 6a and 6b depict instances where the ALS input contains a single tree, which the model accurately approximates, demonstrating its ability to infer complex internal structures from sparse input. Figure 6c further illustrates its performance in closely packed tree settings. Here, ground truth TLS shows four trees with tightly packed canopies, while the model generates fewer distinct trunks than the ground truth. Despite this, the output remains visually realistic and spatially consistent with what a human observer might infer from the incomplete ALS scan.

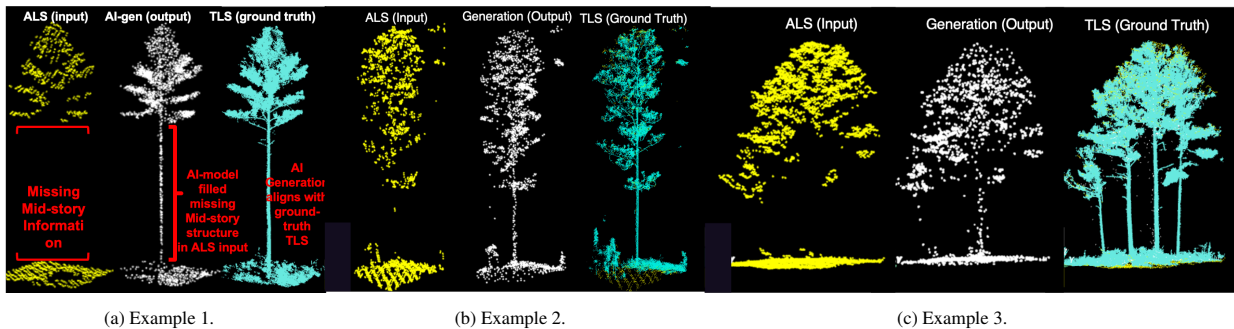


Figure 6: Three examples of DDPM generation at the tree-scale conditioned by ALS inputs in the training set. This qualitative examples showcase the architecture’s capacity to encode and represent the 3D structural details of trees.

Ablation studies to analyze model reconstruction performance were conducted by varying the number of diffusion steps  $T \in \{200, 400, 600, 1000, 2000\}$ , diffusion parameters  $\beta_0 = 10^{-4}$ ,  $\beta_T = 0.02$ , and batch size 16 constant. These experiments aim to analyze the error of the model at training time and also the spatial containment consistency in eq.(2). We track reconstruction error across training iterations using both Chamfer Distance (CD) and Earth Mover’s Distance (EMD), computed between generated and ground-truth TLS point clouds on a held-out validation set of 300 tree examples. As shown in Figs. 7a-7b, both CD and EMD consistently decrease with training iterations across all diffusion schedules, indicating convergence and improving fidelity. Notably, models with higher diffusion steps (e.g.,  $T = 1000$ ) exhibit slower convergence but ultimately achieve slightly lower reconstruction error, while smaller  $T$  values converge quickly with slightly higher error floors.

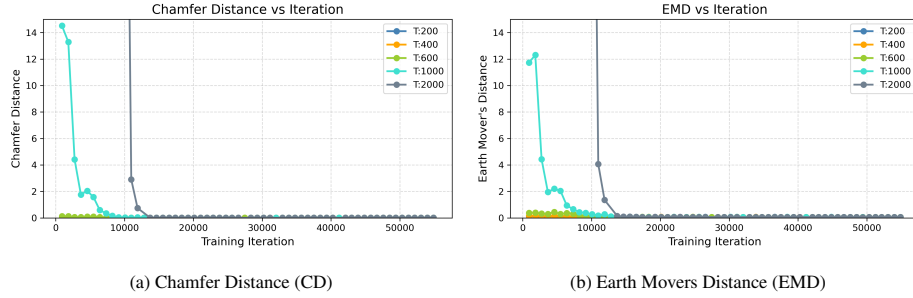


Figure 7: Validation set reconstruction error as a function of training iterations.

In parallel, we assess the containment behavior of generated point clouds using the Expected Point Containment metric, which quantifies the proportion of generated points lying within the ALS convex envelope. Fig. 8a shows that EPC over training iterations mirror reconstruction improvement, suggesting that containment behavior improves with model learning. To investigate the link between spatial consistency and reconstruction fidelity, we plot CD and EMD directly against EPC in Figs. 8b and 8c, respectively. Across all diffusion schedules, we observe a strong inverse correlation: as EPC increases, both CD and EMD rapidly decrease, ultimately plateauing at low error values for high containment ratios. This relationship reveals an important insight: when generated trees remain well contained within the convex hull of ALS inputs, as measured by EPC, this behavior serves as a meaningful indicator of generative quality. In particular, high EPC values consistently appear alongside low reconstruction errors (e.g., CD, EMD), suggesting that EPC can serve as a practical proxy for generation quality in scenarios where ground-truth is unavailable. Moreover, the observed alignment between containment behavior and reconstruction fidelity empirically supports the theoretical guarantee presented in Remark 2.2, demonstrating that the learned conditional distribution  $p_{\theta}(\mathbf{X}|\mathbf{Y})$  inherits the spatial containment property embedded in the training data through ELBO minimization. These findings not only validate our containment assumption, but also highlight its practical utility for model evaluation in operational forest structure generation pipelines lacking TLS ground truth.

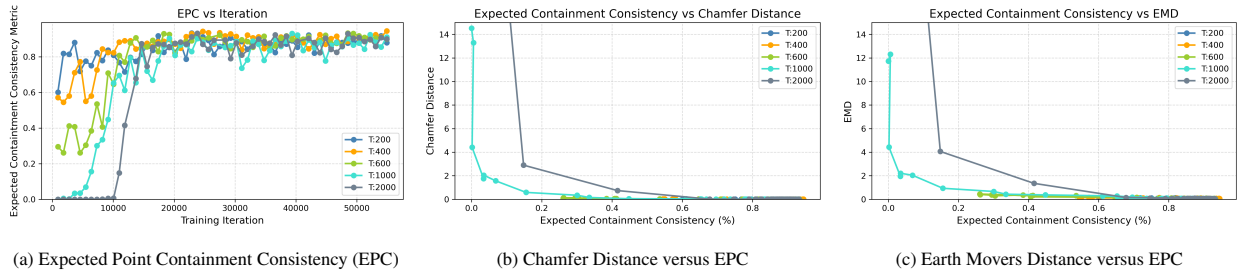


Figure 8: Validation set EPC versus training iteration.

### 3.2. Testing dataset

For testing, we used 50 TLS scans collected from geographic regions entirely outside the training and validation areas, though sharing similar ecosystem characteristics and collected with the same sensors used for the training data. We evaluated the model’s performance across three spatial scales. At the tree scale, we followed the same co-registration and tree detection procedures used during training, resulting in 1,457 individual test trees. This setup enabled direct, one-to-one comparisons between generated samples and corresponding TLS ground truth reference data at high structural fidelity. At the plot scale, we constructed test plots by aggregating ALS data over spatial extents corresponding to each TLS scan, truncating ALS coverage to match the TLS field of view (e.g., 25 meters in radius). This allowed for evaluation of the model’s ability to reconstruct localized forest structure. Finally, at the regional scale, we assessed scalability and extrapolation by deploying the model over multiple 200 meter radius areas containing ALS data. These larger, fully independent areas tested the model’s ability to synthesize realistic vegetation structure

Table 1: Generation/completion errors in test set.

Method	Distance Metrics		
	CD	EMD	EPC (%)
PCN [14]	4.63e-3	9.58e-2	0.921
3D-GAN [15]	4.37e-3	5.761e-2	0.926
<i>l</i> -GAN [16]	6.10e-3	5.59e-2	0.862
PointFlow [17]	4.52e-3	5.429e-2	0.939
ForestGen3D (Ours)	<b>4.30e-3</b>	<b>5.06e-2</b>	<b>0.945</b>

across broader, ALS only landscapes. This evaluation strategy enables comprehensive assessment of ForestGen3D’s robustness and flexibility from fine-grained, tree-level detail to broad-scale generation in mixed conifer ecosystems.

### 3.3. Tree-Scale ALS-Guided Generation

In Fig. 9 we include three representative qualitative comparisons from the test set to illustrate differences between completion/generation approaches across a range of tree structures. First two columns across all three cases represent ALS input and TLS ground truth, while the remaining columns correspond to the completion/generation results. In all three examples, PCN tends to oversmooth crowns, recovering coarse silhouettes while missing high-frequency branching detail. The other baseline generative models (3D-GAN, latent-GAN, and PointFlow) produce shapes that appear closer to the TLS shape, yet are less consistent across examples in general, in comparison to those from our ForestGen3D model. For instance, in the second example, latent-GAN (l) yields a form whose stem does not resemble the straight trunk structure of the TLS reference. Similarly, PointFlow in (f) generates a discontinuous tree stem of larger a diameter compared to ground truth TLS. 3D-GAN and ForestGen3D produce consistently closer results to TLS with canopy structure close to that of ALS and coherent stem-to-crown transitions, recognizable branching patterns, and overall shapes that better match human expectations of realistic tree architecture. These qualitative outcomes mirror the quantitative results below each figure, highlighting the capabilities of generative models to produce realistic structural properties of forests. Note also, that the generated points are generally tightly packed and bounded by the ALS canopy points. This behavior stems from the inherent nature of the ALS training data, where the distribution of the ALS convex-hull is typically broader and encompasses the finer details captured by TLS. Consequently, the generated points do not generally escape the span of the ALS canopy diameter. From a statistical standpoint, as the generative approach aims to produce samples from a distribution that is largely encompassed by the ALS input, it is inherently constrained, making it less likely for the generated points to statistically escape the overall ALS convex envelope.

Table 1 shows a quantitative evaluation summarizing the CD/EMD and EPC metrics over the test dataset of 1457 test examples. This table summarizes the resulting metrics for the completion-based PCN [14] method and the generative models including 3D-GAN [15], latent *l*-GAN [16], PointFlow [17] and our ForestGen3D denoising diffusion based model. For reference, example CD/EMD/EPC values are also reported in Fig. 9 for their corresponding examples. Beyond the numerical values, the metrics highlight important differences between the approaches. PCN, while competitive in CD, performs worst in EMD, reflecting its bias toward capturing coarse, low-frequency geometry at the expense of fine structural detail. Latent-GAN shows the largest CD, due to plausible over-compressing structural features in the latent layers, while 3D-GAN improves CD, it still remains above our model. PointFlow achieves stronger balance across CD and EMD, though it is also higher than the performance of our model. In contrast, ForestGen3D consistently achieves the lowest CD and EMD, while also attaining the highest EPC, indicating superior alignment with TLS reference structure and better recovery of fine-scale details. These results demonstrate that ForestGen3D more effectively learns the underlying distribution of forest structure from ALS–TLS data, achieving overall improved performance compared to both completion/generation-based baselines.

### 3.4. Plot-scale ALS-Guided Generation

We also conduct both qualitative and quantitative analyses at the plot scale, using circular areas with a 25 meter radius. For the qualitative evaluation, we visually compare structural reconstructions obtained from ALS, TLS, ALS+TLS and a hybrid approach combining ALS with ForestGen3D generation enhancement. For each plot, individual

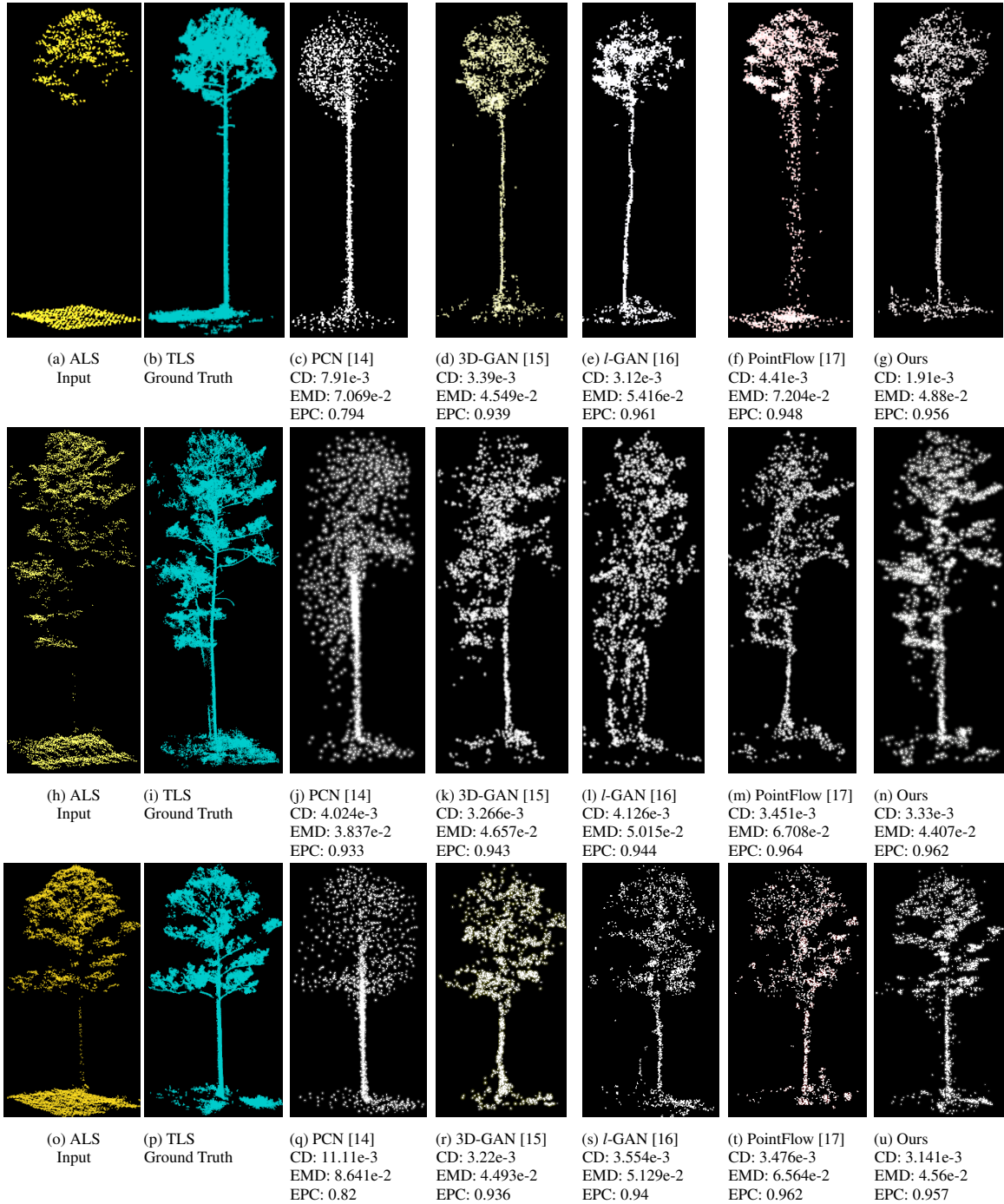


Figure 9: Qualitative comparison of ALS-conditioned tree structure generation across three representative examples. (a,h,o) ALS input and (b,i,p) TLS reference; (c,j,q) PCN [14], (d,k,r) 3D-GAN [15], (e,l,s) latent-GAN [16], (f,m,t) PointFlow [17], and (g,n,u) ForestGen3D (ours). PCN oversmooths crowns, producing coarse silhouettes with little fine-scale detail. The other baselines generate shapes that more closely resemble TLS references but with inconsistencies such as distorted trunks (latent-GAN in (l)) or more discontinuous stems (PointFlow in (f)). 3D-GAN and ForestGen3D yield more coherent reconstructions, with ForestGen3D showing smaller metric errors with respect to ground.

trees were first detected using 3D bounding boxes, and our ForestGen3D model was then applied to generate plausible understory structure beneath each detected tree. Regions lacking tree or shrub like vegetation are left unaltered under the assumption that they do not suffer from occlusion in ALS. To support the quantitative assessment, we perform an evaluation of vegetation biometric estimates derived from each data source: ALS alone, TLS alone, ALS+TLS and ALS enhanced with ForestGen3D. The combined ALS+TLS data serves as ground truth, given its ability to capture detailed, high-resolution vegetation structure across the entire vertical extent of the tree, including the ground, overstory and understory components.

Figure 10 illustrates four representative testset examples (one per row) at plot-scale. The first column illustrates the ALS point cloud, the second column shows the corresponding co-registered ground truth TLS scan, and the third column presents the results of aggregating the ALS scan with the generated under-story from our ForestGen3D model. Note that in all examples, the ALS plots suffer from either missing or highly sparse understory information between the ground and tree foliage, as can be observed in the images in the first column where points are missing. TLS, on the other hand, provides high resolution in the elevation/altitude direction, as shown in the second column, where the main tree stem is finely resolved along the vertical tree-stand direction. The third column, showing the point cloud from ALS+ForestGen3D, illustrates that our approach is capable of enhancing or generating realistic understory structure at the plot scale, where the generated stems and ground features fill in gaps and transition smoothly from the available ALS data.

Building on these qualitative comparisons, we also present Figure 11, which illustrates biophysical tree metrics derived from ALS, TLS, ALS+TLS and ALS+ForestGen3D data sources. This figure offers a histogram per metric (one per sub-column) depicting the distribution of key biophysical tree attributes, offering insight into the variability of tree structures within the sampled region. Such histograms were computed over the individual plots of 25 meter radius. To produce these histograms, we evaluate tree height, diameter at breast height (DBH), crown diameter (CrD), and crown volume (CrV) biometrics using established deep learning-based segmentation methods [19]. These segmentation models first segment each point cloud inside the detected vegetation 3D bounding box, into its structural components: ground, low vegetation, stems, branches and foliage, which are then used as input for geometric fitting techniques that yield the final biophysical metrics.

Tree height was estimated using the highest elevation point in a detected tree and subtracting from it a projection of that point into the ground surface. To estimate DBH, we used the method of [24] on the segmented stem, modifying it for robustness with a RANSAC based linear interpolation of fitted circles along multiple heights around breast height. Note that the RANSAC based fit was used to mitigate the effects of outliers. Crown diameter was estimated by projecting the segmented foliage points onto a 2D plane (collapsing the elevation/altitude dimension) and measuring the maximally distant points in the projection. For crown volume, we employ a  $k$ -means-based convex hull approach, as described in [25]. This method partitions the segmented foliage points into  $k$ -clusters of closely packed 3D points, computes the convex hull of each cluster, and sums the volumes of the  $k$ -clusters. This approach mitigates the effect of including empty-space volume in the calculation, which can occur when applying a single convex hull computation to the full crown structure.

Figure 11 highlights the complementary strengths and inherent limitations of different laser scanning techniques. Among these, the integration of ALS and TLS in the third row across all three examples, offers the most comprehensive view of forest structure, leveraging the wide-area coverage of ALS with the high-resolution, near-ground detail of TLS. This combination enables high-fidelity reconstruction across the entire vertical profile of forest stands above, within, and below the canopy. As such, metrics derived from this data are considered the gold standard reference for evaluating performance across all key biophysical metrics. Individually, ALS in the first row provides efficient and scalable coverage of large landscapes, capturing canopy-top structure effectively from an overhead perspective resulting in estimates without missing information issues for tree height and crown diameter. However, relative to TLS or the ALS+TLS benchmark, ALS alone lacks the resolution necessary to characterize lower-canopy and understory features due to occlusion. This limitation results in poor performance for DBH, with a highly sparse distribution across almost all example cases. Height and crown volume metrics are relatively close to those from the ALS+TLS distributions as they do not heavily depend on the understory information. TLS in the second row across all examples offers fine-grained structural information along the tree-stand direction which results in a denser DBH distribution compared to ALS. In terms of crown diameter we see that the range values in TLS are generally contained within those ALS-derived, this corroborates at the crown level, our assumption that TLS crown points are contained within the corresponding crown points from ALS. In the case of height, the distribution of the TLS-derived height is also

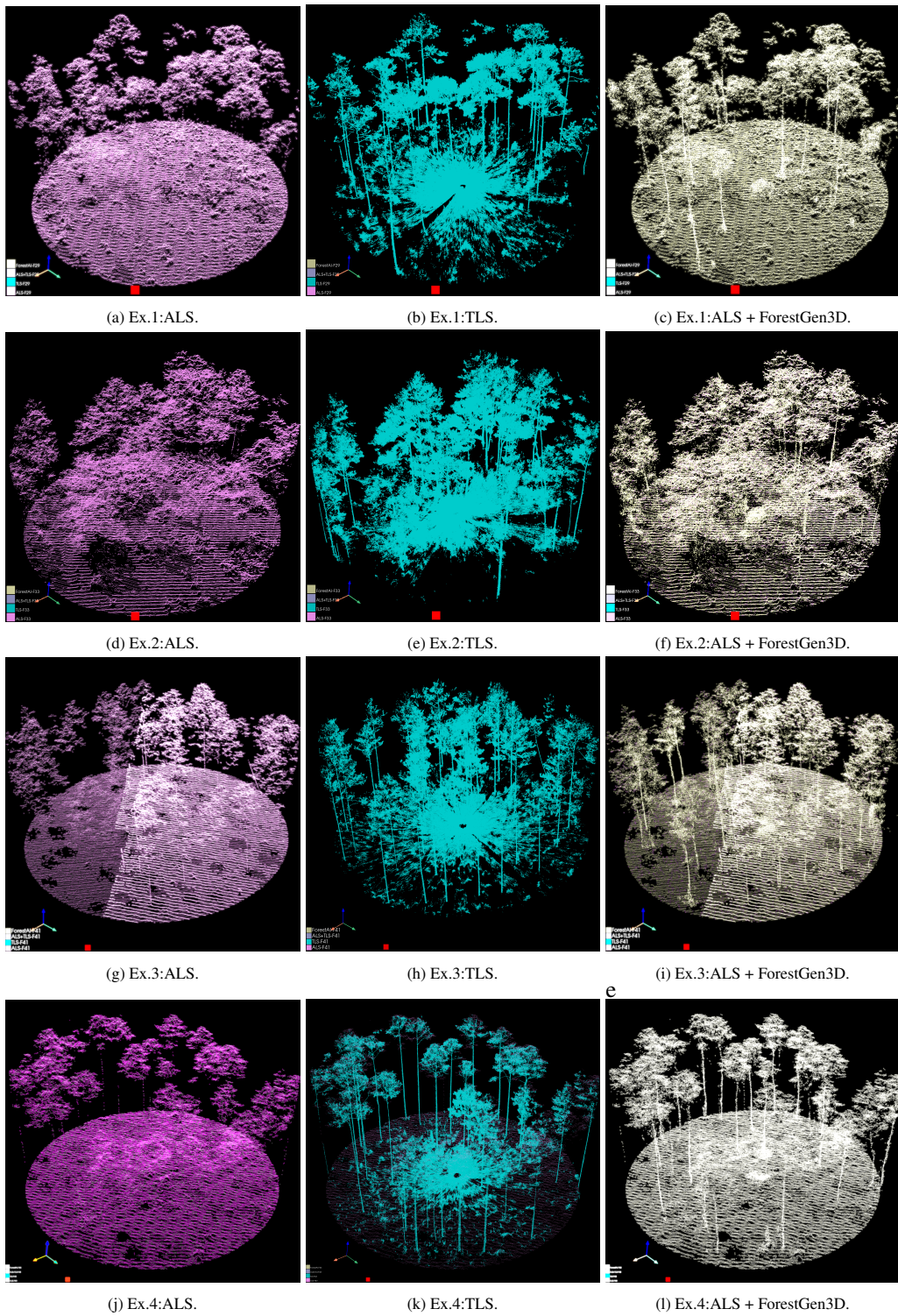


Figure 10: Representative examples comparing 3D structure from ALS, TLS and ALS +ForestGen3D.

Table 2: Plot-scale sensing source biometric distribution differences relative to ALS + ForestGen3D.

Sensing Source	Plot-scale biophysical metrics											
	Example 1				Example 2				Example 3			
	Height	DBH	CrD	CrV	Height	DBH	CrD	CrV	Height	DBH	CrD	CrV
ALS	1.04	0.30	0.79	117.94	0.25	0.18	0.49	44.91	0.29	0.24	1.14	24.20
TLS	1.94	0.23	1.25	98.93	0.30	0.23	0.75	24.82	0.31	0.11	0.84	48.18
ALS + TLS	0.80	0.21	0.85	80.23	0.17	0.18	0.52	11.58	0.12	0.15	0.32	26.8

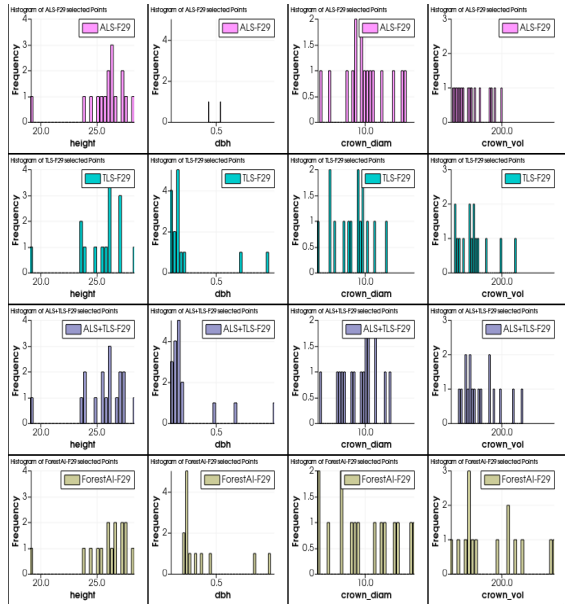
generally contained or similar in range relative to the corresponding ALS-derived. A few heights in the smaller range appear in TLS compared to ALS, coming likely from vegetation/trees under taller trees that ALS did not capture due to occlusion. For the crown volume, a comparison between the ALS and TLS distribution varies since ALS is good at capturing the crown in the lat/long direction whereas TLS is known to capture the crown better in the vertical/elevation direction. Our integrated ALS + ForestGen3D approach in the last row, built with the objective of compensating the structural blind spots of ALS bridges the gap between airborne-scale reach and terrestrial-scale resolution. As observed in the representative examples, the improvements provided by our model produces distributions of biophysical metrics that better approximates the distributions of the gold-standard ALS+TLS. Note also, that in general, the tree height and crown diameter remains approximately contained within that of the corresponding ALS-derived distributions supporting our containment guarantees under ELBO.

Distributional differences in key biophysical metrics: tree height, DBH, CrD, and CrV were also quantified to evaluate model performance. Given the sparse nature of plot-scale biophysical metric distributions (typically 10–30 trees per plot), we employed the Wasserstein distance (WD), which is particularly well suited for such data. This metric offers advantages over alternatives like the Kullback–Leibler divergence, which can become unstable when there is limited overlap between distributions. The Wasserstein distance provides an intuitive and robust measure of distance between two distributions by quantifying the minimum effort required to transform one into the other, and is often also referred to as the Earth Mover’s Distance. We make the distinction, and refer to the metric measuring distance between biometric distributions and the one computing distance over point-clouds for reconstruction error as the EMD. Table 2, compares WD distances between ALS, TLS, and ALS+TLS distributions relative to ALS+ForestGen3D. Each example corresponds to the distributions shown in Figures 11a, 11c, and 11d. Overall, these results consistently show the smallest Wasserstein distances between ALS+ForestGen3D and ALS+TLS, highlighting the model’s effectiveness in generating realistic below-canopy structural information. This leads to biophysical metric distributions that closely resemble those derived from the more comprehensive ALS+TLS data. Further, the distances between ALS+ForestGen3D and the standalone ALS or TLS sources reveal a consistent trend: smaller distances are observed for the source that provides greater information content for the 3D spatial features associated with a given metric. For instance, the distance for the height metric is smaller between ALS+ForestGen3D and ALS than between ALS+ForestGen3D and TLS. This is expected, as ALS is less affected by occlusion in both the ground and crown top regions, making it more uniform and informative for height-related measurements. Finally, note that the scale of the CrV metric is significantly higher than those of height, DBH, and CrD. This is due to the fact that CrV is measured in cubic meters, whereas the other metrics are measures expressed in meters.

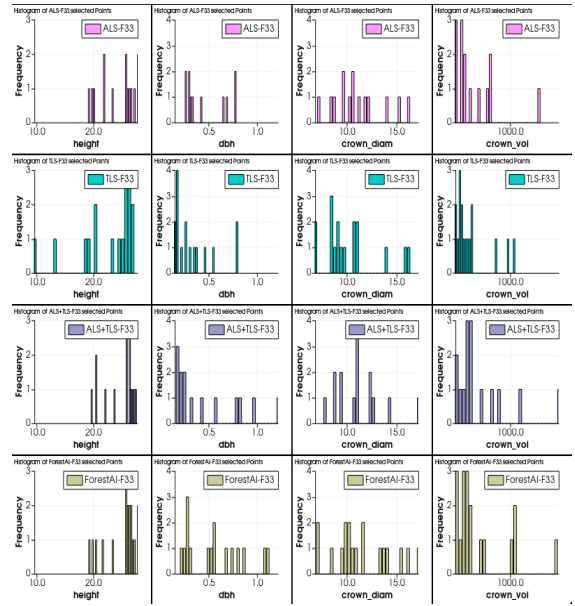
To generalize these findings, Table 3 summarizes the average Wasserstein distances computed over the 51 plots in the testset. This expanded analysis reinforces the trends observed in the examples, confirming that ALS+ForestGen3D distributions most closely match those from ALS+TLS across key biometrics. The consistency of these results across a large number of diverse plots further supports the overall good performance capacity of the ForestGen3D model when the characteristics of the mixed conifer ecosystem remain more or less similar.

### 3.5. Regional-scale ALS-Guided Generation

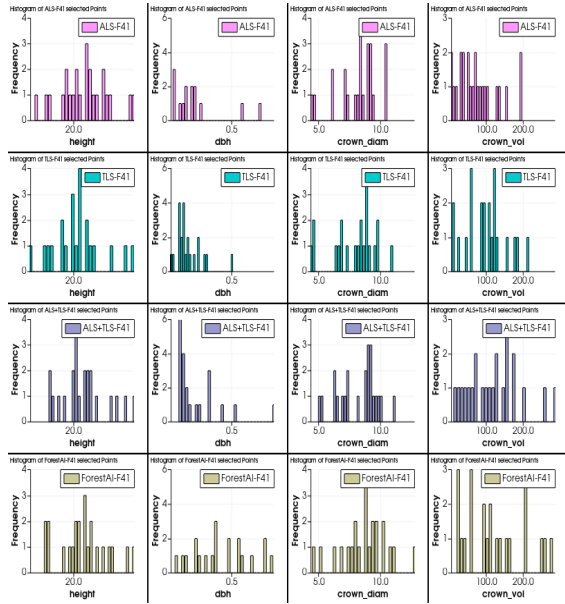
To evaluate the scalability of the ForestGen3D model, we applied it to generate 3D forest structure over a larger spatial extent, a 200-meter radius region centered at a location where a TLS scan is available. While the TLS scan itself covers a range of only 25 meters, this broader area enables us to test the model’s ability to extrapolate beyond small-scale. Notably, the ALS data used in this region was not part of the training set, providing a rigorous test of



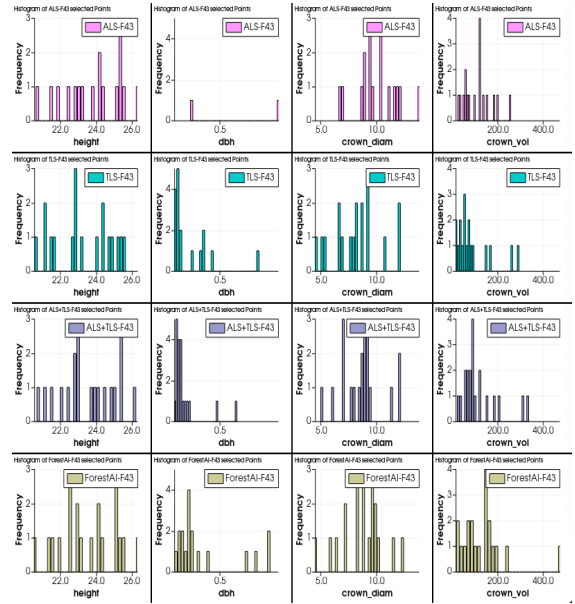
(a) Ex.1 Height (col1), DBH (col2), CrD (col3) and CrV (col4) distribution



(b) Ex.2 Height (col1), DBH (col2), CrD (col3) and CrV (col4) distribution



(c) Ex.3 Height (col1), DBH (col2), CrD (col3) and CrV (col4) distribution



(d) Ex.4 Height (col1), DBH (col2), CrD (col3) and CrV (col4) distribution

Figure 11: Biophysical metric distributions for tree height, DBH, crown diameter and crown volume including comparisons between ALS (row1), TLS (row2), ALS+TLS (row3) and ALS+ForestGen3D (row4).

Table 3: Overall biometric distribution differences between sensing sources relative to ALS + ForestGen3D.

Sensing Source	Plot-scale Biophysical metrics			
	Height	DBH	CD	CV
ALS	1.04	0.30	0.79	117.94
TLS	1.94	0.23	1.25	98.93
ALS + TLS	0.80	0.21	0.85	80.23

the model’s generalization capabilities. The generation procedure at this larger scale mirrors the approach used for plot-level synthesis. First, we apply a tree detection algorithm across the entire ALS region of interest to identify areas with occlusion when viewed from above, which are typically regions where airborne LiDAR fails to resolve understory structure. Second, we extract 3D bounding boxes around these detected trees and apply the ForestGen3D model independently within each bounding box using the local ALS point cloud as input. Finally, the resulting synthetic point clouds are aggregated over the full 200-meter radius area keeping track of their localization to produce a coherent forest-scale 3D reconstruction. Figure 12 illustrate representative snapshot examples of the resulting generation/reconstruction. In these visualizations, point clouds are color-coded as follows: magenta for ALS, turquoise for TLS, peach for ALS + ForestGen3D generation, and white for the generated ForestGen3D sample alone. In this test case where TLS data is not available, the model generates understory structure consistent with the characteristic statistical distribution observed in the training data. Importantly, these large-scale results reflect and reinforce the findings from the plot-scale experiments. ForestGen3D generates foliage and branching structures that blend smoothly into those observed in the ALS data, maintaining spatial consistency and fidelity. In understory regions completely lacking ALS points, the model synthesizes realistic and plausible tree trunks in locations and with diameters that appear structurally consistent with the associated crown geometry provided by ALS. When sparse ALS points are present in the understory, the generated output enhances and complements this limited data by reinforcing plausible stem/branch geometry. At the ground level, the model enriches the representation of shrubs and low vegetation while also improving the resolution of ground returns and the near-ground structure.

To quantitatively assess the generation performance of our model at this landscape scale, we analyzed the EPC metric and the distribution of distances between generated points falling outside the ALS convex envelope and their nearest point on the envelope surface. Figure 13 summarizes this analysis across 10 evaluation plots, each representing a 200 meter radius ALS-only region labeled by plot name on the x-axis. Each violin plot shows the distribution of out-of-envelope distances, computed only for generated points that lie outside the ALS convex hull. The line inside each violin represents the median, while the shape reflects the underlying distance histogram. Text annotations above each violin indicate: (i)  $N$ , the number of trees generated per 200m radius region; (ii) *Out*, the ratio of generated points outside the ALS convex hull (relative to the total number of points); and (iii) the mean  $\pm$  standard deviation of the out-of-envelope distances. Across all plots, the fraction of points outside the ALS envelope remains consistently low, ranging from 1.4% to 1.6%, and mean distances remain below 0.2m. This confirms that the generative model is contained within the implicit ALS spatial convex hull constraints, even in landscape-scale scenarios demonstrating good quality generations via the EPC. The narrow shapes and small deviations provide strong empirical support for our containment assumption and demonstrate that the DDPM model preserves structural plausibility across diverse spatial contexts.

### 3.6. Discussion

Our findings confirm that DDPM models can generate realistic 3D representations of forest tree structures. The model’s ability to preserve fidelity to the true 3D structure depends on the informativeness of additional conditioning data sources. Furthermore, the computational complexity of the generative process scales linearly with area coverage, enabling efficient deployment across large landscapes without increasing model complexity. With current implementations taking  $\approx 2$  seconds per tree-scale generation in a Tesla V100S-PCIE-32GB GPU and with possibilities to further parallelize generation. However, the approach has several limitations. First, the generative model is limited by the distribution it has learned from the training data, which in this case primarily consists of mixed coniferous forest types. When applied to generate trees with structural characteristics not well represented in the training set such as species with drastically different crown architectures, stem densities, branching patterns or ground vegetation (e.g., small shrubs, debris), the model may produce structures that deviate from true vegetation distributions. As a result, generalization to out-of-distribution ecosystems, such as boreal forests, tropical canopies, or hardwood-dominated stands, remains open. Addressing this limitation will require either broadening the training dataset to cover more ecological diversity or incorporating domain adaptation techniques to enable transfer across forest types with different structural priors. While the ALS convex hull provides a useful geometric prior for bounding plausible TLS generation, it is important to note that this containment assumption is approximate. The convex envelope may under/overestimate volume in sparsely sampled regions, and containment does not guarantee structural realism on its own. However, we empirically observe that TLS scans lie within the ALS envelope with over 96% consistency in the training set, and that

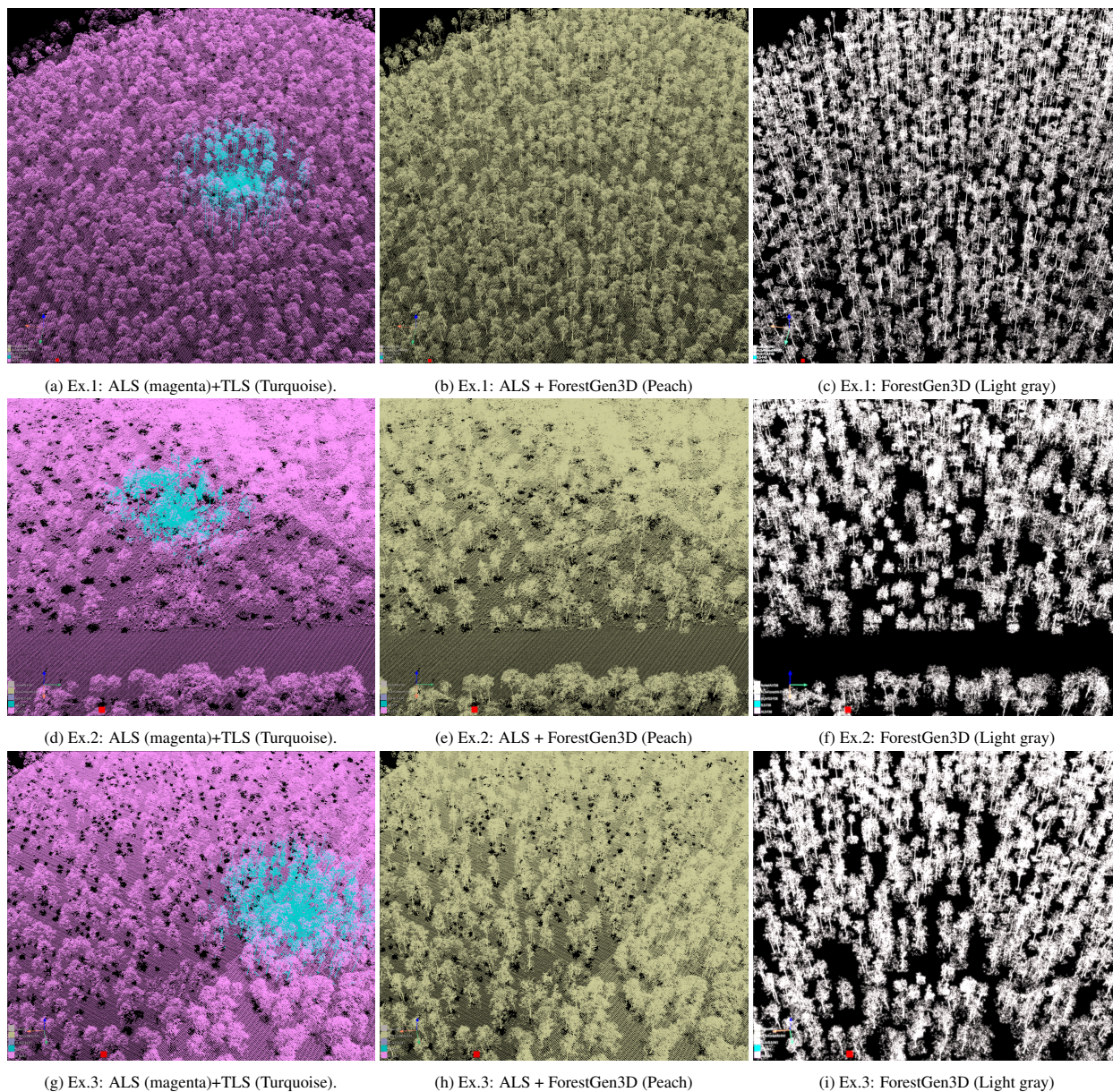


Figure 12: Landscape-scale generation examples from three different areas (one per row). Columns show (a,d,g) broad ALS (magenta) with *in-situ* TLS reference (turquoise), (b,e,h) ALS combined with ForestGen3D output (peach), and (c,f,i) ForestGen3D alone (light gray). Each snapshot corresponds to a circular area of 200 m radius. ForestGen3D was applied selectively to regions with occlusion in ALS, filling in subcanopy structure while leaving unoccluded regions unchanged (black areas indicate no generation). Note that these examples are outside the training set.

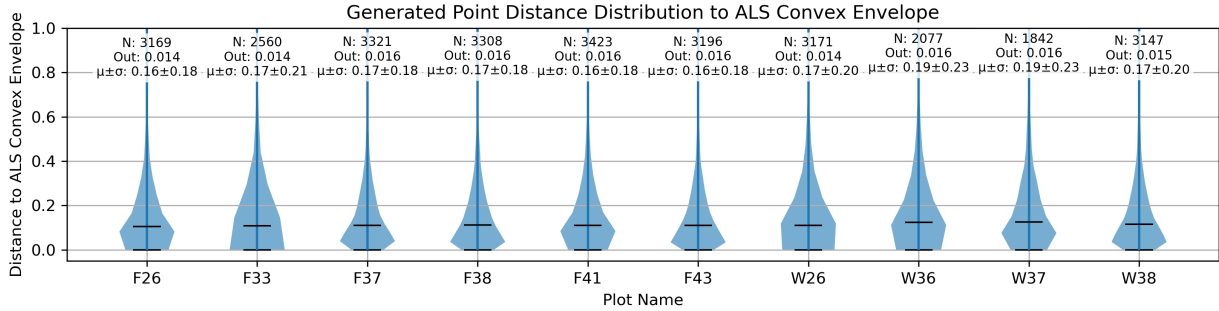


Figure 13: Distribution of distances from generated points to the ALS convex envelope across 10 landscape-scale plots. Each violin plot corresponds to a 200-meter radius region labeled along the x-axis. The y-axis indicates the minimum Euclidean distance from generated points lying outside the ALS convex hull to their nearest point on the hull surface. The violin shape represents the distribution of these distances; the internal black bar denotes the median. Annotations above each plot report:  $N$ , the number of trees generated in the region;  $Out$ , the fraction of generated points falling outside the ALS envelope; and the mean  $\pm$  standard deviation ( $\mu \pm \sigma$ ) of out-of-envelope distances. Across all regions, the proportion of outliers remains below 1.6%, and deviations remain small, typically under 0.2m, indicating strong spatial consistency between the generated structure and the ALS-derived envelope, thus supporting our EPC under ELBO remark.

generation fidelity to the true structure and containment are strongly correlated. These findings support its use as a practical diagnostic metric in large-scale, ground-truth limited deployments.

In dense forest stands, tree detection is often challenged by dense canopies that occlude crown boundaries in ALS data. As a result, the detection pipeline may assign a single bounding box to multiple adjacent trees, which in turn affects the input to the generative model. Depending on the structural cues available in the ALS input, such as crown asymmetry, partial separation, or variations in canopy height the generative model may synthesize either a single fused structure or multiple distinct stems. Because the training dataset includes several examples of closely packed multi-tree configurations, the capacity to distinguish between adjacent trees when sufficient information is present in the point cloud. Nevertheless, in cases where ALS input lacks clear separation cues, the resulting generations may overestimate stem diameter or merge tree forms. To improve robustness in these scenarios, future work will explore both during training and deployment, forest context-aware adaptive tree detection methods, including the use of segmentation masks for individual crown delineation as in [26], as well as stem count aware conditioning strategies to better guide the generative process when multiple trees are present within a single detection. Finally, the model does not explicitly account for temporal variations in forest structure caused by seasonal changes, prescribed burns, wildfires, thinning, or disease. Ignoring these dynamic factors can create a mismatch between generated and real-world forest conditions, limiting the model’s applicability for long-term ecological monitoring and fuel characterization. The aim in future studies is to develop models with additional training/conditional data informative of the potential temporal dynamics either occurring naturally or from human intervention.

Despite these limitations, the ability to reconstruct fine-scale 3D vegetation structure from ALS at the tree, plot and regional scales in mixed conifer ecosystems nonetheless offers immediate utility for existing wildfire modeling frameworks. For example, FastFuels [27] aims to operationalize spatially explicit fuel characterizations by integrating LiDAR and field data through inference-driven mapping. ForestGen3D can complement this by filling in sub-canopy structural gaps where TLS is unavailable, thereby improving vertical fuel profile estimates. Similarly, FIRETEC [28], a physics-based coupled fire-atmosphere model, requires high-resolution 3D inputs that capture canopy gaps, ladder fuels, and understory variation to accurately simulate fire behavior. The generative fidelity of ForestGen3D provides a scalable means to supply such structure across broad landscapes. In addition, QUIC-Fire [29], which enables fast, reduced-order simulations in heterogeneous vegetation, can benefit from ALS-guided 3D generation to populate large domains with spatially consistent and ecologically realistic fuel representations. Integrating ForestGen3D into these modeling frameworks could ultimately support more accurate fire behavior predictions, treatment evaluations, and scenario based risk assessments.

## 4. Conclusion

We present ForestGen3D, a scalable generative modeling framework that produces high-resolution 3D forest structure from aerial LiDAR alone. By leveraging denoising diffusion probabilistic models trained on co-registered aerial and terrestrial LiDAR data, ForestGen3D reconstructs sub-canopy detail that is typically occluded in ALS, enabling realistic and ecologically grounded 3D generations across landscapes. Our work introduces a geometric containment prior, referred to as the expected point consistency, preserved over model generations ensuring spatial plausibility, and we show that this prior can serve as a useful proxy for reconstruction quality in the absence of ground truth TLS. Empirical results across multiple spatial scales confirm that ForestGen3D approximates TLS structure with high fidelity in both geometric and ecological terms. Biophysical metrics derived from generated data such as tree height, DBH, crown diameter, and volume closely match those from full ALS+TLS data, demonstrating the model's utility in ecological monitoring and risk analysis. Despite these strengths, the model's generalizability is constrained by the structural diversity present in the training dataset. Ecosystems with markedly different vegetation forms or disturbance regimes may require adaptation via domain transfer or broader training sets. In addition, the model currently does not explicitly account for temporal dynamics such as seasonal change, management treatments, or natural disturbance recovery. Future work will extend the framework to incorporate more ecosystem diversity, temporal dynamics, and time-aware conditioning to further improve fidelity and robustness. Overall, ForestGen3D provides a practical and extensible solution to the challenge of generating detailed 3D forest structure in ALS-only environments, with promising applications in ecological forecasting, remote sensing, and wildfire modeling.

## Acknowledgement

Research presented in this article was supported by the Laboratory Directed Research and Development program of Los Alamos National Laboratory under project number 20220024DR. This research was also funded by the Department of Defense, Environmental Security Technology Certification Program, grant number RC24-8162. The findings and conclusions in this publication are those of the authors and should not be construed to represent any official USDA or U.S. Government determination or policy.

## References

### References

- [1] P. Köhler, A. Huth, The effects of tree species grouping in tropical rainforest modelling: simulations with the individual-based model formind, *Ecological Modelling* 109 (3) (1998) 301–321.
- [2] S. Dufour-Kowalski, B. Courbaud, P. Dreyfus, C. Meredieu, F. De Coligny, Capsis: an open software framework and community for forest growth modelling, *Annals of forest science* 69 (2012) 221–233.
- [3] L. de Wergifosse, F. André, H. Goosse, A. Boczon, S. Cecchini, A. Ciceu, A. Collalti, N. Cools, E. D'Andrea, B. De Vos, R. Hamdi, M. Ingerslev, M. A. Knudsen, A. Kowalska, S. Leca, G. Matteucci, T. Nord-Larsen, T. G. Sanders, A. Schmitz, P. Termonia, E. Vanguelova, B. Van Schaeybroeck, A. Verstraeten, L. Vesterdal, M. Jonard, Simulating tree growth response to climate change in structurally diverse oak and beech forests, *Science of The Total Environment* 806 (2022) 150422. doi:<https://doi.org/10.1016/j.scitotenv.2021.150422>. URL <https://www.sciencedirect.com/science/article/pii/S0048969721054991>
- [4] I. Maréchaux, F. Langerwisch, A. Huth, H. Bugmann, X. Morin, C. Reyer, R. Seidl, A. Collalti, M. Dantas de Paula, R. Fischer, et al., Tackling unresolved questions in forest ecology: The past and future role of simulation models, *ecol. evol.*, 11, 3746–3770 (2021).
- [5] Interactive Data Visualization, Inc., Speedtree, Interactive Data Visualization, Inc., version 10.x.x (2024). URL <https://store.speedtree.com/>
- [6] U. Technologies, Unity terrain engine, Unity Technologies, part of the Unity engine, for creating terrain (2024). URL <https://unity.com/>
- [7] S. Pokswinski, M. R. Gallagher, N. S. Skowronski, E. L. Loudermilk, C. Hawley, D. Wallace, A. Everland, J. Wallace, J. K. Hiers, A simplified and affordable approach to forest monitoring using single terrestrial laser scans and transect sampling, *MethodsX* 8 (2021) 101484.
- [8] J. Hyypä, H. Hyypä, D. Leckie, F. Gougeon, X. Yu, M. Maltamo, Review of methods of small-footprint airborne laser scanning for extracting forest inventory data in boreal forests, *International Journal of Remote Sensing* 29 (5) (2008) 1339–1366.
- [9] R. Nelson, W. Krabill, G. MacLean, Determining forest canopy characteristics using airborne laser data, *Remote Sensing of Environment* 15 (3) (1984) 201–212.
- [10] C. Mallet, F. Bretar, Full-waveform topographic lidar: State-of-the-art, *ISPRS Journal of photogrammetry and remote sensing* 64 (1) (2009) 1–16.
- [11] J. Castorena, C. D. Creusere, Sampling of time-resolved full-waveform lidar signals at sub-nyquist rates, *IEEE Transactions on Geoscience and Remote Sensing* 53 (7) (2015) 3791–3802.

- [12] K. Calders, J. Adams, J. Armston, H. Bartholomeus, S. Bauwens, L. P. Bentley, J. Chave, F. M. Danson, M. Demol, M. Disney, et al., Terrestrial laser scanning in forest ecology: Expanding the horizon, *Remote Sensing of Environment* 251 (2020) 112102.
- [13] J. Hyyppä, X. Yu, H. Hyyppä, M. Vastaranta, M. Holopainen, A. Kukko, H. Kaartinen, A. Jaakkola, M. Vaaja, J. Koskinen, et al., Advances in forest inventory using airborne laser scanning, *Remote sensing* 4 (5) (2012) 1190–1207.
- [14] W. Yuan, T. Khot, D. Held, C. Mertz, M. Hebert, Pcn: Point completion network, in: 2018 international conference on 3D vision (3DV), IEEE, 2018, pp. 728–737.
- [15] J. Wu, C. Zhang, T. Xue, B. Freeman, J. Tenenbaum, Learning a probabilistic latent space of object shapes via 3d generative-adversarial modeling, *Advances in neural information processing systems* 29 (2016).
- [16] P. Achlioptas, O. Diamanti, I. Mitliagkas, L. Guibas, Learning representations and generative models for 3d point clouds, in: International conference on machine learning, PMLR, 2018, pp. 40–49.
- [17] G. Yang, X. Huang, Z. Hao, M.-Y. Liu, S. Belongie, B. Hariharan, Pointflow: 3d point cloud generation with continuous normalizing flows, in: Proceedings of the IEEE/CVF international conference on computer vision, 2019, pp. 4541–4550.
- [18] J. Castorena, L. T. Dickman, A. J. Killebrew, J. R. Gattiker, R. Linn, E. L. Loudermilk, Forestalign: Automatic forest structure-based alignment for multi-view tls and als point clouds, *Science of Remote Sensing* 11 (2025) 100194.
- [19] L. Windrim, M. Bryson, Forest tree detection and segmentation using high resolution airborne lidar, in: 2019 IEEE/RSJ International Conference on Intelligent Robots and Systems (IROS), IEEE, 2019, pp. 3898–3904.
- [20] M. Snider, S. Pokswinski, S. Wilder, Fort stewart 2025: Contextual data for wildland fire science initiative (wfsi) research burn campaign, WFSI Data Portal (2025). doi:10.60594/W4S88P.
- [21] J. Ho, A. Jain, P. Abbeel, Denoising diffusion probabilistic models, *Advances in neural information processing systems* 33 (2020) 6840–6851.
- [22] Z. Lyu, Z. Kong, X. Xu, L. Pan, D. Lin, A conditional point diffusion-refinement paradigm for 3d point cloud completion, arXiv preprint arXiv:2112.03530 (2021).
- [23] C. R. Qi, L. Yi, H. Su, L. J. Guibas, Pointnet++: Deep hierarchical feature learning on point sets in a metric space, *Advances in neural information processing systems* 30 (2017).
- [24] B. Rijal, A. R. Weiskittel, J. A. Kershaw Jr, Development of height to crown base models for thirteen tree species of the north american acadian region, *The Forestry Chronicle* 88 (1) (2012) 60–73.
- [25] Z. Zhu, C. Kleinn, N. Nölke, Assessing tree crown volume—a review, *Forestry: An International Journal of Forest Research* 94 (1) (2021) 18–35.
- [26] J. Yang, Z. Kang, S. Cheng, Z. Yang, P. H. Akwensi, An individual tree segmentation method based on watershed algorithm and three-dimensional spatial distribution analysis from airborne lidar point clouds, *IEEE Journal of Selected Topics in Applied Earth Observations and Remote Sensing* 13 (2020) 1055–1067.
- [27] A. Marozzi, L. Wells, R. Parsons, E. Mueller, R. Linn, J. K. Hiers, Fastfuels: Advancing wildland fire modeling with high-resolution 3d fuel data and data assimilation, *Environmental Modelling and Software* 183 (2025) 106214. doi:10.1016/j.envsoft.2024.106214. URL <http://dx.doi.org/10.1016/j.envsoft.2024.106214>
- [28] R. Linn, J. Reisner, J. J. Colman, J. Winterkamp, Studying wildfire behavior using firetec, *International journal of wildland fire* 11 (4) (2002) 233–246.
- [29] R. R. Linn, S. L. Goodrick, S. Brambilla, M. J. Brown, R. S. Middleton, J. J. O’Brien, J. K. Hiers, Quic-fire: A fast-running simulation tool for prescribed fire planning, *Environmental Modelling and Software* 125 (2020) 104616.
- [30] T. M. Cover, J. A. Thomas, *Elements of Information Theory*, 2nd Edition, Wiley-Interscience, 2006.

## Appendix A: Soft Containment Guarantee via ELBO Minimization

**Assumptions.** Let  $(\mathbf{X}_0, \mathbf{Y})$  denote a paired TLS–ALS point cloud sample drawn from the empirical training distribution  $\mathcal{D}$ . Let  $\mathcal{B}_{\text{ALS}}(\mathbf{Y}) = \text{Conv}(\mathbf{Y})$  denote the convex hull of the ALS point cloud. Define the point-level containment indicator  $C(\mathbf{x}, \mathbf{Y}) = 1(\mathbf{x} \in \mathcal{B}_{\text{ALS}}(\mathbf{Y}))$ .

We assume:

1. **Empirical containment:** TLS points are spatially bounded by the ALS convex hull in expectation:

$$\mathbb{E}_{(\mathbf{X}_0, \mathbf{Y}) \sim \mathcal{D}} [\mathbb{E}_{\mathbf{x} \sim \mathbf{X}_0} [C(\mathbf{x}, \mathbf{Y})]] \geq 1 - \epsilon$$

for a small constant  $\epsilon \in [0, 1]$ .

2. **Model approximation:** The learned model  $p_\theta(\mathbf{X}_0 | \mathbf{Y})$  satisfies a KL divergence bound:

$$\text{KL}(p_{\text{data}}(\mathbf{X}_0 | \mathbf{Y}) \| p_\theta(\mathbf{X}_0 | \mathbf{Y})) \leq \delta_{\text{KL}}$$

for all  $\mathbf{Y}$ .

**Scope Note.** The containment assumption stated above is specific to the tree scale, where  $(\mathbf{X}_0$  and  $\mathbf{Y})$  are co-registered ALS and TLS point clouds corresponding to individual trees or small tree clusters. We do not assume global containment over entire plots or landscape-scale point clouds, where occlusion and ALS sparsity can invalidate this

condition. In our dataset, this per-tree containment assumption is empirically validated, with over 96% of TLS points contained within the ALS convex hull on average.

**Goal.** Show that the expected containment of generated points satisfies:

$$\mathbb{E}_{\mathbf{Y}} \left[ \mathbb{E}_{\mathbf{X}_0 \sim p_{\theta}(\cdot | \mathbf{Y})} \left[ \mathbb{E}_{\mathbf{x} \sim \mathbf{X}_0} [C(\mathbf{x}, \mathbf{Y})] \right] \right] \geq 1 - \epsilon - \delta$$

for some  $\delta = \sqrt{2\delta_{\text{KL}}}$ , using Pinsker’s inequality.

**Proof.** Let

$$f(\mathbf{X}_0, \mathbf{Y}) = \mathbb{E}_{\mathbf{x} \sim \mathbf{X}_0} [C(\mathbf{x}, \mathbf{Y})]$$

be the average containment score for a TLS sample  $\mathbf{X}_0$  with respect to the ALS envelope. By assumption (1), we have:

$$\mathbb{E}_{(\mathbf{X}_0, \mathbf{Y}) \sim \mathcal{D}} [f(\mathbf{X}_0, \mathbf{Y})] \geq 1 - \epsilon.$$

Now fix a conditioning ALS point cloud  $\mathbf{Y}$ . Then:

$$\left| \mathbb{E}_{\mathbf{X}_0 \sim p_{\text{data}}(\cdot | \mathbf{Y})} f(\mathbf{X}_0, \mathbf{Y}) - \mathbb{E}_{\mathbf{X}_0 \sim p_{\theta}(\cdot | \mathbf{Y})} f(\mathbf{X}_0, \mathbf{Y}) \right| \leq \|p_{\text{data}}(\cdot | \mathbf{Y}) - p_{\theta}(\cdot | \mathbf{Y})\|_{\text{TV}}.$$

Here,  $\|\cdot\|_{\text{TV}}$  denotes the total variation norm, a standard metric between probability distributions. It bounds the discrepancy in expectations of bounded functions and is upper-bounded by KL divergence via Pinsker’s inequality [30]. Applying such inequality:

$$\|p_{\text{data}}(\cdot | \mathbf{Y}) - p_{\theta}(\cdot | \mathbf{Y})\|_{\text{TV}} \leq \sqrt{\frac{1}{2} \text{KL}(p_{\text{data}} \| p_{\theta})} \leq \sqrt{\frac{1}{2} \delta_{\text{KL}}}.$$

Since  $f$  is bounded in  $[0, 1]$ , we obtain:

$$\mathbb{E}_{\mathbf{X}_0 \sim p_{\theta}(\cdot | \mathbf{Y})} f(\mathbf{X}_0, \mathbf{Y}) \geq \mathbb{E}_{\mathbf{X}_0 \sim p_{\text{data}}(\cdot | \mathbf{Y})} f(\mathbf{X}_0, \mathbf{Y}) - \sqrt{\frac{1}{2} \delta_{\text{KL}}}.$$

Taking the expectation over  $\mathbf{Y}$  and combining with the empirical containment assumption:

$$\mathbb{E}_{\mathbf{Y}} \left[ \mathbb{E}_{\mathbf{X}_0 \sim p_{\theta}(\cdot | \mathbf{Y})} f(\mathbf{X}_0, \mathbf{Y}) \right] \geq \mathbb{E}_{\mathbf{Y}} \left[ \mathbb{E}_{\mathbf{X}_0 \sim p_{\text{data}}(\cdot | \mathbf{Y})} f(\mathbf{X}_0, \mathbf{Y}) \right] - \sqrt{2\delta_{\text{KL}}} \geq 1 - \epsilon - \sqrt{2\delta_{\text{KL}}}.$$

Therefore:

$$\mathbb{E}_{\mathbf{Y}} \left[ \mathbb{E}_{\mathbf{X}_0 \sim p_{\theta}(\cdot | \mathbf{Y})} \left[ \mathbb{E}_{\mathbf{x} \sim \mathbf{X}_0} [1(x \in \mathcal{B}_{\text{ALS}}(\mathbf{Y}))] \right] \right] \geq 1 - \epsilon - \sqrt{2\delta_{\text{KL}}}.$$

□

## Appendix B: Unconditional 3D Tree Generation with DDPM

In some regions, TLS or co-registered ALS–TLS data may be unavailable due to logistical constraints, cost, or historical limitations. In such cases, it becomes necessary to resort to statistical approximations such as species specific structural priors or to borrow training data from ecologically similar surrogate areas. One advantage of the proposed DDPM framework is that it supports unconditional generation, allowing plausible 3D vegetation structure to be synthesized even without ALS guidance. This is particularly useful in applications where only species composition, vegetation type, or biophysical statistical information is known to populate a geo-referenced region. We include here several illustrative examples at the tree-scale that demonstrate that the model, even in the absence of ALS conditioning, can produce tree structures that are structurally realistic and ecologically consistent with those found in the training distribution.

Figure .14 presents ten illustrative samples from the model, trained on the 2900 extracted trees from TLS scans without using ALS conditioning. The generated tree structures exhibit fine details along the vertical tree-stand direction, mirroring the characteristics of the TLS training data. The model successfully learns the spatial distribution of key tree components: trunk, branches, leaves, and ground, along with their spatial relationships. Additionally, the model captures variations in canopy structure despite being trained on a relatively small dataset. The generated trees predominantly resemble mixed conifer species, including longleaf, slash, and loblolly pines, reflecting their prevalence in the training dataset. To the best of our knowledge, this model achieves an unprecedented level of detail in tree generation directly from real LiDAR forestry data.

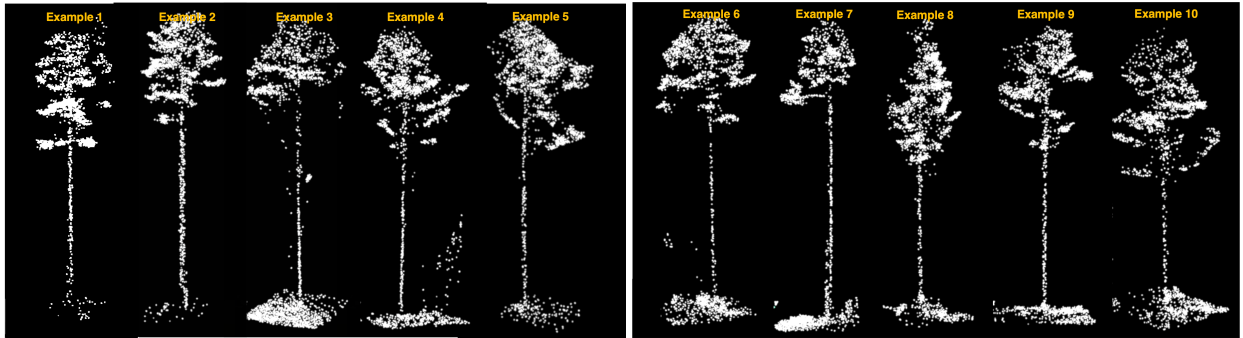
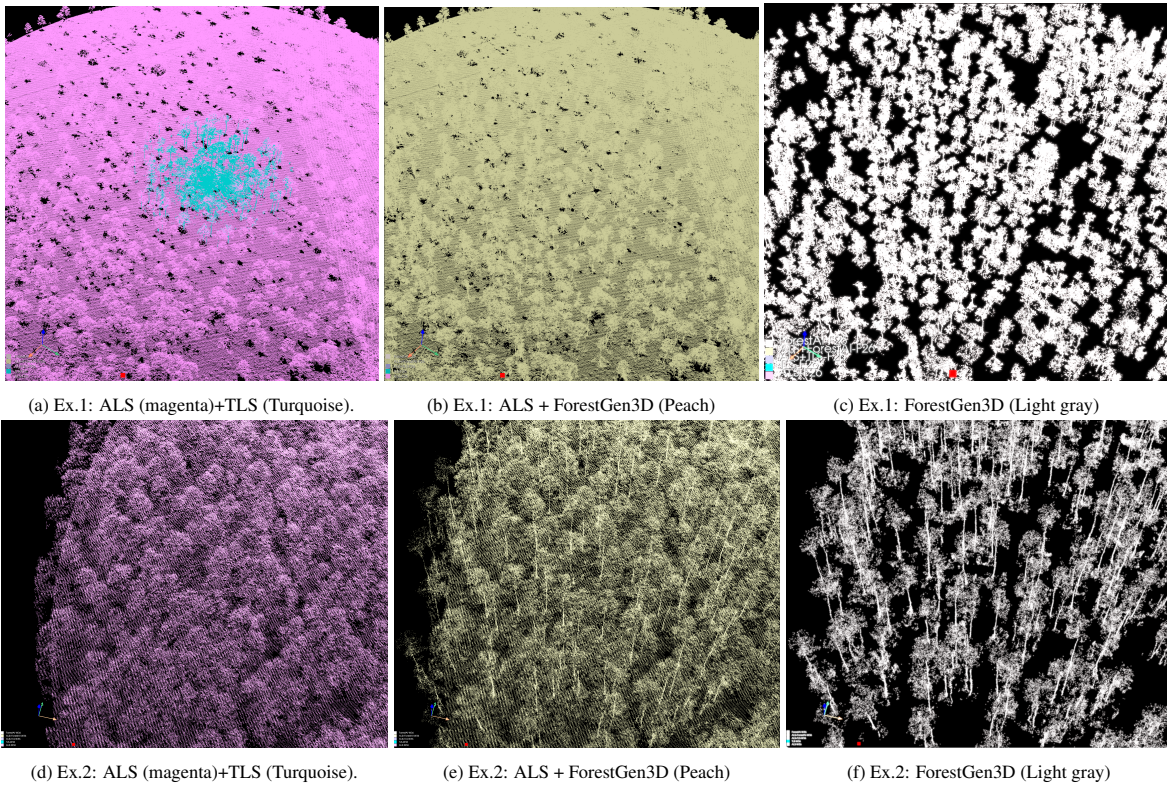


Figure .14: DDPm model generation under unconditional setting: Sample from Gaussian distribution and generate tree structures according to a training TLS scan dataset.

### Appendix C: Additional Regional-scale Generations

This section just presents a few more illustrations of the generation performance of our ForestGen3D model at the regional scale. The included Figures below are spatial snapshots of the 200m radius regions. In these figures, the sources are color-coded as: magenta for ALS, turquoise for TLS, peach for ALS + ForestGen3D generation, and white for the generated ForestGen3D sample alone.



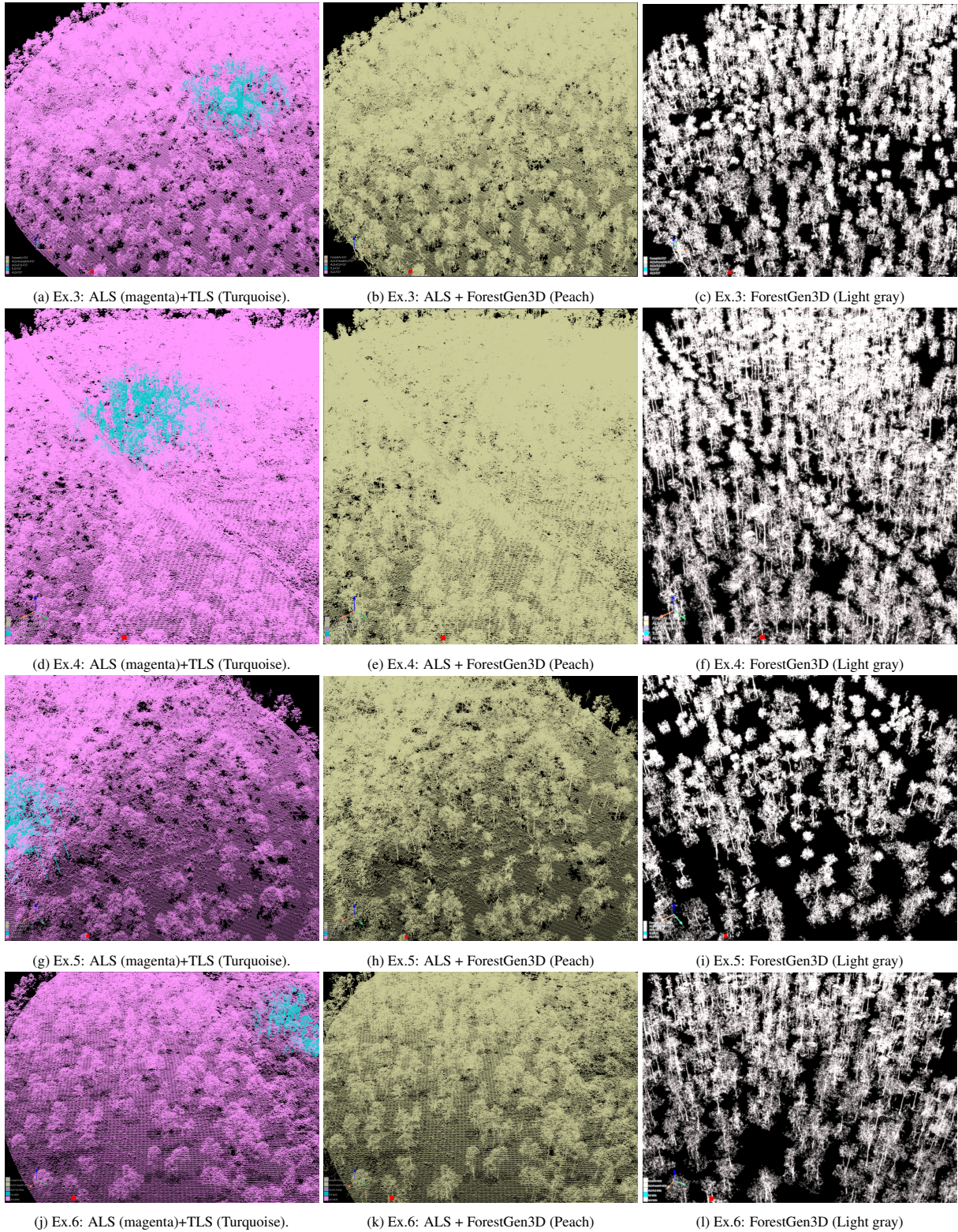


Figure .16: Additional examples of landscape generation with fidelity to ALS scan inputs. Here the ForestGen3D model was targeted only to regions where there is occlusion from vegetation and from an aerial perspective.